Non-intrusive reduced order modelling of the Navier–Stokes equations

D. Xiao [a,d], F. Fang [a,*], A.G. Buchan [a], C.C. Pain [a], I.M. Navon [b], A. Muggeridge [c]

[a] [1] *Applied Modelling and Computation Group, Department of Earth Science and Engineering, Imperial College London, Prince Consort Road, London, SW7 2BP, UK*
[b] *Department of Scientific Computing, Florida State University, Tallahassee, FL, 32306-4120, USA*
[c] *Department of Earth Science and Engineering, Imperial College, London SW7 2BP, UK*
[d] *China University of Geosciences, Wuhan, 430074, China*

Highlights

- This is the first work to apply two non-intrusive ROMs for solving the N–S equations.
- A second order Taylors series method for calculating the POD coefficients.
- A Smolyak sparse grid collocation method for calculating the POD coefficients.
- Implementation of the non-intrusive ROMs does not require modifications to a system code.
- Ability of non-intrusive ROMs to capture the highly nonlinear fluid dynamics.

Abstract

This article presents two new non-intrusive reduced order models based upon proper orthogonal decomposition (POD) for solving the Navier–Stokes equations. The novelty of these methods resides in how the reduced order models are formed, that is, how the coefficients of the POD expansions are calculated. Rather than taking a standard approach of projecting the underlying equations onto the reduced space through a Galerkin projection, here two different techniques are employed. The first method applies a second order Taylor series to calculate the POD coefficients at each time step from the POD coefficients at earlier time steps. The second method uses a Smolyak sparse grid collocation method to calculate the POD coefficients, where again the coefficients at earlier time steps are used as the inputs. The advantage of both approaches are that they are non-intrusive and so do not require modifications to a system code; they are therefore very easy to implement. They also provide accurate solutions for modelling flow problems, and this has been demonstrated by the simulation of flows past a cylinder and within a gyre. It is demonstrated that accuracy relative to the high fidelity model is maintained whilst CPU times are reduced by several orders of magnitude in comparison to high fidelity models.

---

* Corresponding author.

E-mail address: f.fang@imperial.ac.uk (F. Fang).
[1] URL: http://amcg.ese.imperial.ac.uk.

1. Introduction

Reduced order models (ROMs) have become prevalent in many fields of physics as they offer the potential to simulate dynamical systems with substantially increased computation efficiency in comparison to standard techniques. Among the model reduction techniques, the proper orthogonal decomposition (POD) method has proven to be an efficient means of deriving a reduced basis for high-dimensional nonlinear flow systems. The POD method has been successfully applied to numerous research fields and has a number of variants, such as the principal component analysis (PCA) method [1] in statistics; Karhunen–Loeve method [2] in signal analysis and pattern recognition; and empirical orthogonal functions (EOF) [3,4] in geophysical fluid dynamics and meteorology. The POD method has also been applied to ocean models in Cao et al. [5], Vermeulen and Heemink [6] and also to shallow water equation models. Its application includes the work of Daescu and Navon [7], Stefanescu et al. [8,9], Chen et al. [10,11], Altaf et al. [12], Du et al. [13], Fang et al. [14], as well as Xiao et al. [15,16].

However in most cases the source code describing the physical model has to be modified in order to generate the reduced order model. These modifications can be complex, especially in legacy codes, or may not be possible if the source code is not available (*e.g.* in some commercial software) [17]. To circumvent these shortcomings, more recently, non-intrusive methods have been introduced into ROMs, which do not require the knowledge of the governing equations and the original code [17]. Noack [18] and Noori [19] introduced the Neural Network into ROMs. Chen [17] proposed a Black Box Stencil interpolation non-intrusive method, which is based on parametric regression methods, and applied it to a one dimensional chemical reaction problem and two dimensional porous media flow problems. Audouze et al. [20] proposed a non-intrusive Radial Basis Function (RBF) reduced-order modelling method for approximating the solutions of nonlinear time-dependent parameterized partial differential equations (Burgers' equation and a parameterized convection–reaction–diffusion problem). Iuliano and Quagliarella [21] developed a non-intrusive POD ROM for aerodynamic shape optimization. Guénot et al. [22], Casenave et al. [23] and Klie [24] proposed a non-intrusive POD ROM based on RBF and the EIM/DEIM algorithm. However, most of current non-intrusive ROMs may still suffer from prohibitive computational costs due to the exponential increase of the number of multidimensional functions with the dimensional size of problems (in ROM, the dimensional size $d = P \times N_v$, where P is the number of POD bases and N_v is the number of variables to be solved).

To cope with the curse of dimensionality, as we know, the Smolyak sparse grid method [25] is an efficient method of integrating/interpolating multidimensional functions based on a univariate quadrature rule. This sparse grid method has been widely applied in various applications [26–28], including numerical integration [29], partial differential equations [30], economics [31,32], stochastic natural convection problems [33], sensitivity analysis [34], portfolio problems [35] and high dimensional interpolation [36].

To our best knowledge, little attempt has been made to use the sparse grid method in ROMs with exception of Peherstorfer [37], Cheng [38], Ullmann [39] and Lang, and Sumant [40]. Peherstorfer [37] presented a reduced-order model of parameterized systems by employing a sparse grid machine learning method and applied this new ROM to thermal conduction and chemical reaction simulations. Sumant [40] used a Smolyak algorithm to compute orthogonal polynomial expansions coefficients in the reduction of random input variables for an electromagnetic problems. Cheng [38] presented a method for numerical simulation of the stochastic Berger equation, and investigated the sparsity property in terms of Karhunen–Loeve expansions. Ullmann [39] and Lang assessed the applicability of POD/Galerkin to stochastic collocation on the sparse grid.

This paper presents the first work to apply non-intrusive ROMs to the Navier–Stokes equations. These ROMs are implemented here within a high fidelity unstructured mesh fluid model. The ability of non-intrusive ROMs to capture the highly nonlinear fluid dynamics is investigated here. The first non-intrusive ROM uses a sparse grid collocation approach (based on Smolyak grids) and another is derived using Taylor series expansion. The reduced order models are constructed using a finite element Bubnov–Galerkin discretization of the Fluidity fluid dynamics modelling software [41] taking snapshots of the solution variables at regular time intervals. In the Smolyak sparse grid ROM approach, solutions of the full model are recorded (as a sequence of snapshots), and from this data appropriate basis functions are formed that optimally represent the problem. The Smolyak sparse grid method is used to construct interpolation functions that approximate the non-linearity of the model. In the Taylor/POD approach, the model based on snapshots is expanded through a Taylor expansion to second order so as to capture the quadratic non-linearities in the high fidelity system.

The structure of the paper is as follows. Section 2 presents the governing equations, followed by the derivation of the standard POD model reduction. Section 3 presents the non-intrusive method based on the second order Taylor series theory. Section 4 presents the Smolyak sparse grid method in reduced order modelling. Section 5 demonstrates the method's capabilities by solving two problems. Finally in Section 6, the summary and conclusions are presented.

2. Reduced order modelling of the Navier–Stokes equations

2.1. Governing equations

This article considers the three dimensional non-hydrostatic Navier–Stokes equations describing the conservation of mass and momentum of a fluid,

$$\nabla \cdot \mathbf{u} = 0, \tag{1a}$$

$$\frac{\partial \mathbf{u}}{\partial t} + \mathbf{u} \cdot \nabla \mathbf{u} + f \mathbf{k} \times \mathbf{u} = -\nabla p + \nabla \cdot \boldsymbol{\tau}. \tag{1b}$$

In these equations the term $\mathbf{u} \equiv (u_x, u_y, u_z)^T$ denotes the velocity vector, p the perturbation pressure ($p := p/\rho_0$, ρ_0 is the constant reference density) and f the Coriolis inertial force. The stress tensor $\boldsymbol{\tau}$ included in the diffusion term represents the viscous forces, and this is defined in terms of a deformation rate tensor $\mathbf{S}$ which is given by,

$$\tau_{ij} = 2\mu_{ij} S_{ij}, \quad S_{ij} = \frac{1}{2}\left(\frac{\partial u_i}{\partial x_j} + \frac{\partial u_j}{\partial x_i}\right) - \frac{1}{3}\sum_{k=1}^{3}\frac{\partial u_k}{\partial x_k}, \quad i, j = \{x, y, z\}. \tag{2}$$

In this expression μ denotes the kinematic viscosity and it is assumed that there is no summation over repeated indices. The horizontal (μ_{xx}, μ_{yy}) and vertical (μ_{zz}) kinematic viscosities are assumed to take constant values and define the off diagonal components of $\boldsymbol{\tau}$ in Eq. (2) by $\mu_{ij} = (\mu_{ii}\mu_{jj})^{1/2}$. For barotropic flow, the pressure p consists of hydrostatic $p_h(z)$ and non-hydrostatic $p_{nh}(x, y, z, t)$ components.

2.2. Reduction via proper orthogonal decomposition

2.2.1. Proper orthogonal decomposition

In the POD formulation a new set of basis functions is constructed from a collection of snapshots that are taken at a number of time instances of the full model solution. The model described in Eqs. (1a) and (1b) are solved and snapshots of the solution are taken as it evolves through time. In the formulation presented here snapshots of each component of the velocity vector $\mathbf{u} = (u_x, u_y, u_z)$ and pressure p are recorded individually. Each snapshot is a vector of size $\mathcal{N}$ and holds the values of the respective solution component at the nodes of the finite element mesh. For each velocity or pressure component, the sampled values at the snapshot s are stored in the vectors $\mathcal{U}_s^x$, $\mathcal{U}_s^y$, $\mathcal{U}_s^z$ and $\mathcal{U}_s^p$ (where the superscripts denote space direction or pressure) with $\mathcal{N}$ entries ($\mathcal{N}$ being the number of nodes). A collection of all $\mathcal{U}_s^x$, $\mathcal{U}_s^y$, $\mathcal{U}_s^z$ and $\mathcal{U}_s^p$ constructs four separate matrices $\mathcal{U}^x = (\mathcal{U}_1^x, \ldots, \mathcal{U}_s^x, \ldots, \mathcal{U}_S^x)$, $\mathcal{U}^y = (\mathcal{U}_1^y, \ldots, \mathcal{U}_s^y, \ldots, \mathcal{U}_S^y), \mathcal{U}^z = (\mathcal{U}_1^z, \ldots, \mathcal{U}_s^z, \ldots, \mathcal{U}_S^z)$ and $\mathcal{U}^p = (\mathcal{U}_1^p, \ldots, \mathcal{U}_s^p, \ldots, \mathcal{U}_S^p)$ respectively (where S is the number of snapshots). From here on each snapshot matrix will be treated separately, but in an identical manner, and so the superscripts are omitted for the sake of simplicity of notation and the details are provided for a general snapshot matrix $\mathcal{U}$.

Taking the deviation from the mean forms a modified snapshot matrix $\tilde{\mathcal{U}}$ by,

$$\tilde{\mathcal{U}}_s = \mathcal{U}_s - \overline{\mathcal{U}}, \quad s \in \{1, 2, \ldots, S\}, \tag{3}$$

where

$$\overline{\mathcal{U}} = \frac{1}{S}\sum_{s=1}^{S}\mathcal{U}_s. \tag{4}$$

The goal of POD is to find a set of orthogonal basis functions $\{\phi_s\}$, $s \in \{1, 2, \ldots, S\}$, such that it maximizes

$$\frac{1}{S} \sum_{s=1}^{S} \left| < \tilde{\mathcal{U}}_s, \phi_s >_{L^2} \right|^2, \tag{5}$$

subject to

$$\sum_{s=1}^{S} | < \phi_s, \phi_s >_{L^2} |^2 = 1, \tag{6}$$

where $\langle \cdot, \cdot \rangle_{L^2}$ is the canonical inner product in L^2 norm.

The approach introduced by Sirovich [42] is used to find an optimal set of basis functions Φ of the optimization problem (5). This involves performing a Singular Value Decomposition (SVD) of the snapshot matrix $\tilde{\mathcal{U}}$ given in the form,

$$\tilde{\mathcal{U}} = U \Sigma V^T. \tag{7}$$

The terms $U \in R^{\mathcal{N} \times \mathcal{N}}$ and $V \in R^{S \times S}$ are the matrices that consist of the orthogonal vectors for $\tilde{\mathcal{U}}\tilde{\mathcal{U}}^T$ and $\tilde{\mathcal{U}}^T\tilde{\mathcal{U}}$, respectively and Σ is a diagonal matrix of size $\mathcal{N} \times S$. The non zero values of Σ are the singular values of $\tilde{\mathcal{U}}$, and these are assumed to be listed in order of their decreasing magnitude. It can be shown [43] that the POD vectors are defined to be the column vectors of the matrix V,

$$\phi_s = \tilde{\mathcal{U}} V_{:,s} / \sqrt{\lambda_s}, \quad \text{for } s \in \{1, 2 \ldots S\}, \tag{8}$$

and the optimal basis set of size P consists of the functions corresponding to the largest P singular values (*i.e.* the first P columns of U). These vectors are optimal in the sense that no other rank P set of basis vectors can be closer to the snapshot matrix $\tilde{\mathcal{U}}$ in the Frobenius norm.

In POD, any variable ψ (for example, the velocity and pressure components) can be expressed by the expansion,

$$\psi = \overline{\psi} + \sum_{j=1}^{P} \alpha_j \phi_j, \tag{9}$$

where α_j denote the coefficients of the POD expansion and $\overline{\psi}$ is the mean of the ensemble of snapshots for the variable ψ.

As a final note, the loss of information due to the truncation of the POD expansion set to P vectors can be quantified by the following ratio,

$$I = \frac{\sum_{j=1}^{P} \lambda_j^2}{\sum_{j=1}^{S} \lambda_j^2}, \tag{10}$$

where λ denotes singular values. The value of I will tend to 1 as P is increased to the value S, which would imply no loss of information.

2.2.2. Implementation of a standard (Galerkin projection) POD reduced order model

For simplicity Eqs. (1a) and (1b) can be re-written in the general form:

$$\frac{\partial \psi}{\partial t} = F(\psi). \tag{11}$$

Taking the POD basis function as the test function, then integrating (11) over the computational domain Ω, yields:

$$\left\langle \frac{\partial \psi}{\partial t}, \phi_j \right\rangle_{\Omega} = \langle F(\psi), \phi_j \rangle_{\Omega}. \tag{12}$$

Substituting (9) into (12), the POD reduced order equations are then obtained:

$$\frac{\partial \alpha_k}{\partial t} = \left\langle F\left(\bar{\psi} + \sum_{j=1}^{P} \alpha_j \phi_j\right), \phi_k \right\rangle_{\Omega}, \quad \text{for } k \in \{1, 2 \ldots P\}, \tag{13}$$

subject to the initial condition

$$\alpha_k(t) = ((\psi(t) - \bar{\psi}), \phi_k), \quad at \ t = 0. \tag{14}$$

Eq. (13) at time level n can be written:

$$\frac{\alpha_k^n - \alpha_k^{n-1}}{\Delta t} = \left\langle F\left(\bar{\psi} + \sum_{j=1}^{P} \alpha_j^{n-1} \phi_j\right), \phi_k \right\rangle_{\Omega}, \quad \text{for } k \in \{1, 2 \ldots P\}, \tag{15}$$

where Δt is the time step size to be used. Eq. (15) can be rewritten in the general form below:

$$\alpha_k^{n+1} = f_k(\alpha^n), \quad k \in \{1, 2, \ldots, P\}. \tag{16}$$

In this work, alternative approaches are sought for quickly estimating the multidimensional functions f_k in (16). This enables us to then estimate the POD coefficients of the reduced order model at arbitrary times. The first of these methods is implemented through a Taylor series expansion and the second is through a Smolyak sparse grid method. These are detailed in the following sections.

3. The Taylor series method for the calculation of the POD coefficients

3.1. Taylor expression of the POD Coefficients

For a new time step, say $n + 2$, a first order Taylor expansion of the POD coefficients $\boldsymbol{\alpha}^{n+2} = (\alpha_1^{n+2}, \ldots, \alpha_P^{n+2})^T$ (where $\boldsymbol{\alpha}$ denotes the complete set of coefficients for velocity and pressure) can be written as,

$$\boldsymbol{\alpha}^{n+2} = \boldsymbol{\alpha}^{n+1} + \frac{\partial \boldsymbol{\alpha}^{n+1}}{\partial \boldsymbol{\alpha}^n}(\boldsymbol{\alpha}^{n+1} - \boldsymbol{\alpha}^n), \tag{17}$$

in terms of the POD coefficients on the previous two time steps. The term $(\boldsymbol{\alpha}^{n+1} - \boldsymbol{\alpha}^n)$ denotes the change in coefficient values over time steps $n + 1$ and n, where $n \in \{1, 2, \ldots, N\}$ (N is the total number of time levels). Due to the Navier–Stokes equations having quadratic non-linearities, it is more appropriate to extend this Taylor expansion to second order accuracy,

$$\boldsymbol{\alpha}^{n+2} = \boldsymbol{\alpha}^{n+1} + \left(M_0 + \sum_{k=1}^{P}(\boldsymbol{\alpha}_k^{n+1} - \boldsymbol{\alpha}_k^n)M_k\right)(\boldsymbol{\alpha}^{n+1} - \boldsymbol{\alpha}^n), \tag{18}$$

which is expressed in terms of matrices M_0 and M_k, for $k \in \{1, 2, \ldots, P\}$, that have dimensions $P \times P$. These denote the derivatives of the POD coefficients at one time step with respect to a change in the POD coefficients at the previous time step. The matrix M_0 holds the first order derivatives and is given by,

$$(M_0)_{i,j} = \frac{\partial \boldsymbol{\alpha}_i^{n+1}}{\partial \boldsymbol{\alpha}_j^n} \approx \frac{\partial \boldsymbol{\alpha}_i^1}{\partial \boldsymbol{\alpha}_j^0}, \quad i, j \in \{1, 2, \ldots, P\}, \tag{19}$$

whereas the matrices M_k contain the second order derivatives which are given by,

$$(M_k)_{i,j} = \frac{\partial^2 \boldsymbol{\alpha}_i^{n+1}}{\partial \boldsymbol{\alpha}_j^n \partial \boldsymbol{\alpha}_k^n} \approx \frac{\partial^2 \boldsymbol{\alpha}_i^1}{\partial \boldsymbol{\alpha}_j^0 \partial \boldsymbol{\alpha}_k^0}, \quad i, j, k \in \{1, 2, \ldots, P\}. \tag{20}$$

Note that the matrices M_0 and M_k, for $k \in \{1, 2, \ldots, P\}$ are assumed to be constant in time and so can be pre-calculated. Once the solutions $\boldsymbol{\alpha}^0$ and $\boldsymbol{\alpha}^1$ at the first two time instances $t = 0, 1$ are determined, the POD coefficients at time level n can be estimated from Eq. (17).

3.2. Offline calculation of the first and second derivative matrices in the Taylor series

An efficient way to calculate the derivative matrices M_0 and M_k, for $k \in \{1, 2, \ldots, P\}$ is through a perturbation of the POD coefficients at one time instance. Suppose the perturbation vector is $\boldsymbol{\Delta\alpha}_j^0 = (0, \ldots, \delta\alpha_j^0, \ldots, 0)^T$ for a perturbation $\delta\alpha_j^0$ of the jth entry in α^0, then the ith element of the computed POD vector $\hat{\alpha}^1$ at time instance 1 will provide the variation of the ith POD coefficient with respect to the change in α^0. This can be used to compute the first derivative matrix, M_0 through the relationship:

$$(M_0)_{i,j} = \frac{\hat{\boldsymbol{\alpha}}_i^1 - \boldsymbol{\alpha}_i^1}{\delta\alpha_j^0}, \quad i, j \in \{1, 2, \ldots, P\}. \tag{21}$$

The perturbed solutions $\hat{\alpha}^1$ at time step 1 can be thus calculated using the following process:

(a) Map the vectors $\alpha^0 + \boldsymbol{\Delta\alpha}_j^0$ to the full space, then obtain the perturbed initial solution $\hat{\psi}^0 = \overline{\psi} + \sum_{j=1}^{P}(\alpha^0 + \boldsymbol{\Delta\alpha}_j^0)\phi_j$;

(b) Calculate the solution at the next time step, $\hat{\psi}^1$, through running the full model one time instance;

(c) Obtain the perturbed POD vector $\hat{\alpha}_i^1$ by projecting $\hat{\psi}^1$ onto the reduced space, $\hat{\alpha}^1 = \phi^T \hat{\psi}^1$.

The whole matrix M_0 can be computed by repeating the process P times and perturbing each POD coefficient α_j^0 ($j \in \{1, 2, \ldots, P\}$) in turn.

The calculation of the second derivative matrix M_k in (20) follows an extended route similar to that used in the generation of the matrix M_0. For each k, two perturbed vectors are created, $\hat{\alpha}_k^{0,+}$ and $\hat{\alpha}_k^{0,-}$, which have small positive and negative perturbations in the kth entry of the original vector α^0, i.e. $\hat{\alpha}_k^{0,\pm} = \alpha^0 \pm \boldsymbol{\Delta\alpha}_k^0$, where, $\boldsymbol{\Delta\alpha}_k^0 = (0, \ldots, \delta\alpha_k^0, \ldots, 0)^T$. Using these two vectors, two first order derivative matrices are generated using the process described above, these are denoted M_k^+ and M_k^- and have elements defined as,

$$(M_0)_{i,j}^{\pm} = \frac{\partial\boldsymbol{\alpha}_i^{\pm,1}}{\partial\boldsymbol{\alpha}_j^{\pm,0}} \quad i, j \in \{1, 2, \ldots, P\}. \tag{22}$$

The second order derivatives are formed from the two Taylor expansions,

$$(M_k)_{i,j}^{\pm} = (M_0)_{i,j} \pm \frac{\partial}{\partial\boldsymbol{\alpha}_k^0}(M_0)_{i,j}\|\delta\alpha_k^0\|, \tag{23}$$

which, by subtracting one from the other, can be re-arranged to form,

$$(M_k) = \frac{1}{2\|\delta\alpha_k\|}(M_k^+ - M_k^-). \tag{24}$$

4. The Smolyak sparse grid method for calculating the POD coefficients

The Smolyak sparse grid algorithm is an efficient method that is used to solve high dimensional linear tensor product problems. Using the Smolyak method, the interpolation function values need to be determined only at the sparse grid mesh points rather than on the full tensor product grid, thus resulting in an impressive computational economy in comparison to tensor product evaluations, as the number of points no longer increases exponentially with the dimensional size d. In this work, the Smolyak sparse grid interpolation method [25] is used to construct a set of interpolating multidimensional functions $\hat{f}_k$, ($k \in \{1, 2, \ldots, P\}$) for representing the functions f_k in Eq. (16).

4.1. The Smolyak sparse grid algorithm

Let $\hat{f}_k^{d,l}$ denote a Smolyak interpolant of dimension d with an approximational level l, which is a linear combination of tensor product operators:

$$\hat{f}_k^{d,l}(\alpha^n) = \sum_{max(d,l+1)\leq|\mathbf{l}|\leq d+l} (-1)^{d+l-|\mathbf{j}|} \cdot \binom{d-1}{d+l-|\mathbf{i}|} (U^{i_1} \otimes \cdots \otimes U^{i_d}) f(\alpha^n), \tag{25}$$

where $|\mathbf{i}| = i_1 + \cdots + i_d$ (here $i_1, \ldots, i_d$ are indices in each dimension respectively), $(-1)^{d+l-|\mathbf{i}|} \cdot \binom{d-1}{d+l-|\mathbf{i}|}$ is a counting coefficient. The tensor product operator of a d-dimensional function f_k is defined as:

$$(U_k^{i_1} \otimes \cdots \otimes U^{i_d})(f_k) = \sum_{j_1=1}^{O_{l_1}} \cdots \sum_{j_d=1}^{O_{i_d}} f_k(x_{j_1}^{i_1}, \ldots, x_{j_d}^{i_d}).(P_{j_1}^{i_1} \otimes \cdots \otimes P_{j_d}^{i_d}), \tag{26}$$

where $P_{j_1}^{i_1}, P_{j_2}^{i_2}, \ldots, P_{j_d}^{i_d}$ are the basis functions and $O_{l_1}, O_{l_2} \ldots O_{l_d}$ are the number of basis functions used in each dimension with $O_{i_d} = 2^{i_d-1} + 1$ respectively, $f(x_{j_1}^{i_1}, \ldots, x_{j_d}^{i_d})$ represents the function value at $(x_{j_1}^{i_1}, \ldots, x_{j_d}^{i_d})$, and $i_d = 1, 2, \ldots, O_{l_d}$.

4.2. The calculation of the POD coefficients

A set of Smolyak interpolation functions $\hat{f}_k^{d,l}(\alpha^n)$ in the form of (25) is now used to estimate the POD coefficient α_k^n at time level $n+1$,

$$\alpha_k^{n+1} = \hat{f}_k(\alpha^n), \quad k \in \{1, 2, \ldots, P\}, \tag{27}$$

where the spatial dimensional size d equals the size of the reduced order space (*i.e.* the number of POD bases P). The input for each interpolation function $\hat{f}_k(\alpha^n)$ is the complete set of POD coefficients $\alpha^n = (\alpha_1^n, \alpha_2^n, \ldots, \alpha_P^n)$ at the previous times step n. The output of $\hat{f}_k^{d,l}(\alpha^n)$ is the kth POD coefficient α^{n+1} at time step $n+1$, *i.e.*,

$$\hat{f}_k^{d,l}(\alpha^n) : \alpha^n \to \alpha_j^{n+1}, \quad k \in \{1, 2, \ldots, P\}. \tag{28}$$

The Smolyak interpolation functions $\hat{f}_k^{d,l}(\alpha^n)$ are calculated offline using the functional values at the Smolyak grids. Each interpolation function denotes a supercube surface or a P-dimensional super surface. Once the interpolation functions are constructed, the POD coefficients at the current timestep $n+1$ are obtained by entering the POD coefficients at the previous timestep n into the interpolation functions.

The offline calculation of the Smolyak interpolation functions $\hat{f}_k^{d,l}(\alpha^n)$ can be described as follows:

(a) Choose a set of sparse interpolation grids $\alpha^{r,0} = (\alpha_1^{r,0}, \alpha_2^{r,0}, \ldots, \alpha_P^{r,0})$ (where $r \in \{1, 2, \ldots, R\}$, R is the number of sparse grids to be chosen), which lie in some product interval
$[A_{min}, A_{max}] = [\alpha_{1,min}, \alpha_{1,max}] \ldots \otimes [\alpha_{j,min}, \alpha_{j,max}] \ldots \otimes [\alpha_{P,min}, \alpha_{P,max}]$
(where $\alpha_{k,min}$ and $\alpha_{k,max}$ are the minimum and maximum values of the kth POD coefficient, $k \in \{1, 2, \ldots, P\}$);
(b) Calculate a corresponding set of the function value $\alpha_k^{r,1} = f_k(\alpha^{r,0})$ located at the sparse grids through running the full model one time step from time level 0 to 1:
 (i) Determine the initial condition $\psi^{r,0}$ for the full model by projecting $\alpha^{r,0}$ onto the full space, where ψ denotes any variable in the full model, for example, the velocity components u_x, u_y and u_z, and the pressure p;
 (ii) Determine the full solution $\psi^{r,1}$ by running the full model one time level;
 (iii) Calculate the function value $\alpha_j^{r,1}$ at sparse grid r by projecting $\psi^{r,1}$ onto the reduced order space;
 (iv) Repeat the above procedures (i)–(iii) and obtain all the function values at the sparse grids $r \in \{1, 2, \ldots, R\}$;
(c) Given a set of $\alpha_j^{r,1}$, construct the interpolation function $\hat{f}_k^{d,l}(\alpha^n)$, $k \in \{1, 2, \ldots, P\}$.

5. Numerical examples

A demonstration of the use of the non-intrusive POD reduced order modelling schemes is presented in this section. This numerical illustration consists in solving two problems. In one we model flow past a cylinder and in the other we model flow within a gyre. We used the Arpack package to perform the singular Value Decomposition and, in particular, to obtain the leading singular value. The Smolyak grid was determined using the "SPARSE_INTERP_ND Multidimensional Sparse Interpolant" authored by Burkardt [28,44] whilst the original fine grid simulations were calculated using Fluidity [41]. These provided the exact solutions for model comparison, as well as the snapshots for the POD function generation.

In this demonstration a comparison between the full model and the non-intrusive model reduction approach has been made. In addition to comparing solution profiles the analysis compares the solution root mean square errors, as well as correlation coefficients. The measured error is given by the root mean square error (RMSE) which is calculated for each time step n by,

$$RMSE^n = \sqrt{\frac{\sum_{i=1}^{F}(\psi_i^n - \psi_{o,i}^n)^2}{F}}. \tag{29}$$

In this expression ψ_i^n and $\psi_{o,i}^n$ denote the POD (mapped onto the full mesh) and the full model solution at the node i, respectively, and F represents the number of nodes on the full mesh. The correlation coefficient is computed for each time step, and is defined for given expected values μ_{ψ^n} and $\mu_{\psi_o^n}$ and standard deviations σ_{ψ^n} and $\sigma_{\psi_o^n}$,

$$corr(\psi^n, \psi_o^n)^n = \frac{cov(\psi^n, \psi_o^n)}{\sigma_{\psi^n}\sigma_{\psi_o^n}} = \frac{E(\psi^n - \sigma_{\psi^n})(\psi_o^n - \sigma_{\psi_o^n})}{\sigma_{\psi^n}\sigma_{\psi_o^n}}, \tag{30}$$

where E denotes mathematical expectation, cov denotes covariance, σ denotes standard deviation.

5.1. Case 1: Flow past a cylinder

We illustrate the novel non-intrusive methods via two numerical examples. Both cases typify non-laminar flows. In the first numerical example a two dimensional flow past a cylinder is simulated. In fluid dynamics, vortex shedding is an oscillating flow that takes place when a fluid such as air or water flows past a cylindrical body at certain velocities, depending on the size and shape of the body. These are called Von Karman vortices.

The problem domain is 2 units in length and 0.4 units in width, and it contains a cylinder of radius 0.12 units at location (0.2, 0.2). The dynamics of the fluid flow are caused by a slightly compressible fluid flowing through the domain with a velocity 1. This enters the domain through the left boundary. The fluid is allowed to flow past the cylinder and out of the domain through the right boundary. No slip and zero outward flow conditions are applied to the upper and lower edges of the problem, whilst Dirichlet boundary conditions are applied to the cylinder's wall. From the full model simulation, with a mesh of 3213 nodes, 400 snapshots were obtained at regularly spaced time intervals $\Delta t = 0.02$ for each of the u, v and p solution variables.

In order to evaluate the capabilities and the difference between the Smolyak sparse grid ROM and the Taylor expansion POD model, two cases one with a Reynolds number of 400 and the other with a Reynolds number of 3600 were investigated. The simulation period is $[2 - 10]$, and a time step of $\Delta t = 0.01$ was used for all models.

Fig. 1 shows the solutions for the flow past the cylinder at time instances 3.0 and 10.0, as calculated using the two non-intrusive models (Smolyak sparse grid ROM and Taylor/POD model respectively), the full high fidelity model and the standard (Galerkin projection) POD model using 12 POD basis functions. The Reynolds number was 400 in this case. These solutions show that all methods have performed particularly well at resolving the flow at both time instances. This is highlighted further in Fig. 2 which presents the solution velocities predicted by all methods at the position (0.19397, 0.28101) on the domain. It can be seen from this figure that the Smolyak sparse grid ROM is in closer agreement with the full model, whilst both the standard and Taylor POD models are able to capture the wave pattern, but have a large error near the peak of waves during the spin-up period of modelling, *i.e.* [200, 550]. It is shown the Smolyak sparse grid ROM can perform better than other POD models since it is highly customizable through the choice of admissible multi-index sets and well converges to the tensor product of exact operators [45].

To further demonstrate the capability of the non-intrusive models, the Reynolds number was then increased to $Re = 3600$. Visual inspection of Fig. 3 shows that decrease of eigenvalues satisfies exponential Kolmogorov n-width. This helps us to choose the number of POD bases. The more number of POD bases are chosen, the more energy is captured. In this case, 12, 24 and 35 POD bases are used to demonstrate the performance of ROM.

The comparison of results between the full and POD models (the standard, Taylor and Smolyak sparse grid non-intrusive POD models) was carried out. Fig. 4 shows the simulated flow patterns at time instances 3.0 and 10.0 (where 12 POD bases are used). As shown in the figures the Smolyak sparse grid non-intrusive model performs well for this Reynolds number. However, it can be seen that the Taylor/POD non-intrusive model does not capture well the complex flow patterns and eddies for this high Reynolds number while the standard POD model has a large error near

(a) full model, $t = 3.0$.

(b) full model, $t = 10.0$.

(c) standard POD, $t = 3.0$.

(d) standard POD, $t = 10.0$.

(e) Taylor/POD, $t = 3.0$.

(f) Taylor/POD, $t = 10.0$.

(g) Smolyak sparse grid ROM, $t = 3.0$.

(h) Smolyak sparse grid ROM, $t = 10.0$.
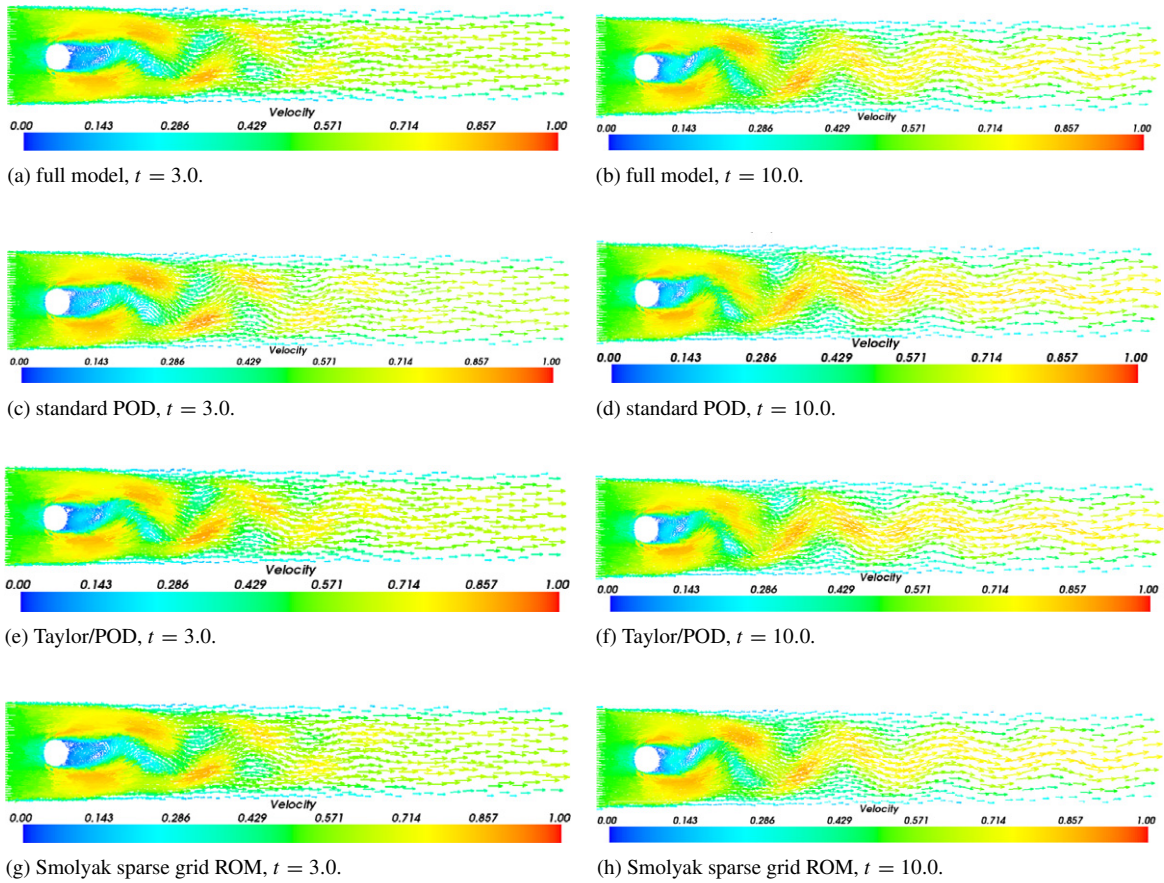
Fig. 1. Case one—flow past a cylinder at $Re = 400$: The figures displayed above show the solutions of the flow past a cylinder problem at time instances 3.0 and 10.0. The solutions compare the predictions from non-intrusive models (Smolyak sparse grid ROM and Taylor/POD) with full model and standard (Galerkin projection) POD model using 12 POD bases functions.
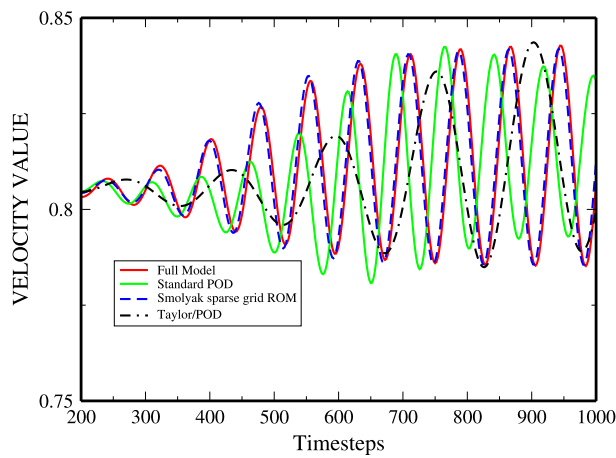
Fig. 2. Case one—flow past a cylinder: The graphs show the solution velocities predicted by the full model, POD model, Taylor expansion method and the Smolyak sparse grid ROM at positions: 0.19397, 0.28101, Re = 400.

the cylinder. Fig. 5 shows the difference between the full model and Smolyak sparse grid and standard POD of the flow past a cylinder problem at time instances 3.0 and 10.0 using 12 and 24 POD basis functions, respectively. The
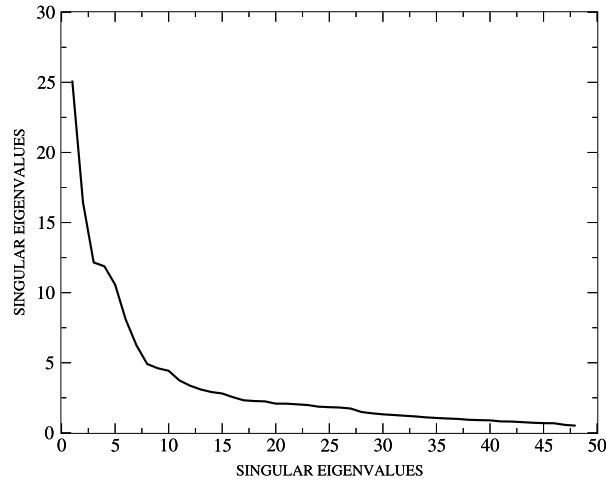
Fig. 3. Case one—flow past a cylinder at $Re = 400$: The graphs show the singular eigenvalues in order of decreasing magnitude.

(a) full model, $t = 3.0$.

(b) full model, $t = 10.0$.

(c) standard POD, $t = 3.0$.

(d) standard POD, $t = 10.0$.

(e) Taylor/POD, $t = 3.0$.

(f) Taylor/POD, $t = 10.0$.

(g) Smolyak sparse grid ROM, $t = 3.0$.

(h) Smolyak sparse grid ROM, $t = 10.0$.
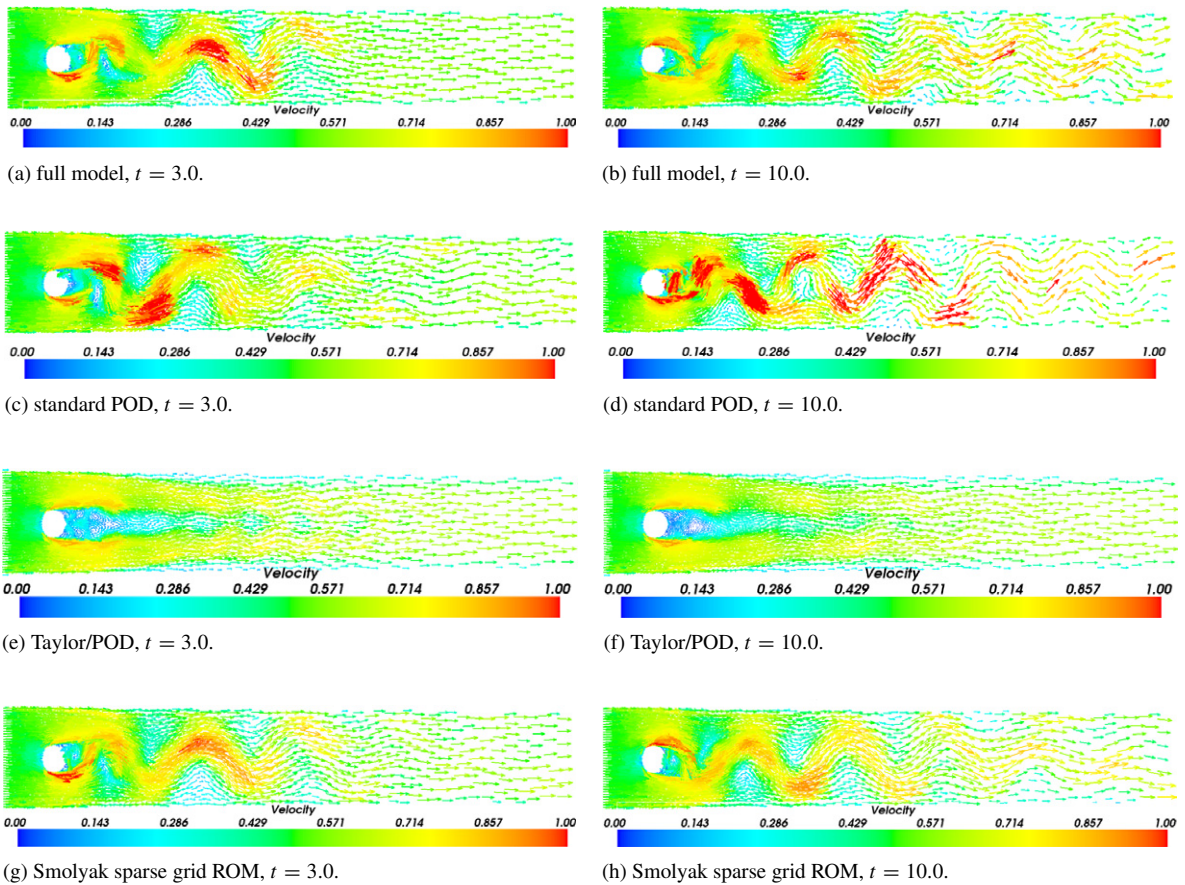
Fig. 4. Case one—flow past a cylinder at $Re = 3600$: The figures displayed above show the solutions of the flow past a cylinder problem at time instances 3.0 and 10.0. The solutions compare the predictions from Smolyak sparse grid ROM and Taylor/POD non-intrusive models with the full model and the standard POD model using 12 POD basis functions.

figures illustrate the fact that the error between the full model and the Smolyak sparse grid ROM is smaller than that between full model and the standard POD model.

(a) standard POD error, $t = 3.0$, 12 POD bases.

(b) standard POD error, $t = 10.0$, 12 POD bases.

(c) standard POD error, $t = 3.0$, 24 POD bases.

(d) standard POD error, $t = 10.0$, 24 POD bases.

(e) Smolyak/POD error, $t = 3.0$, 12 POD bases.

(f) Smolyak/POD error, $t = 10.0$, 12 POD bases.

(g) Smolyak/POD error, $t = 3.0$, 24 POD bases.

(h) Smolyak/POD error, $t = 10.0$, 24 POD bases.
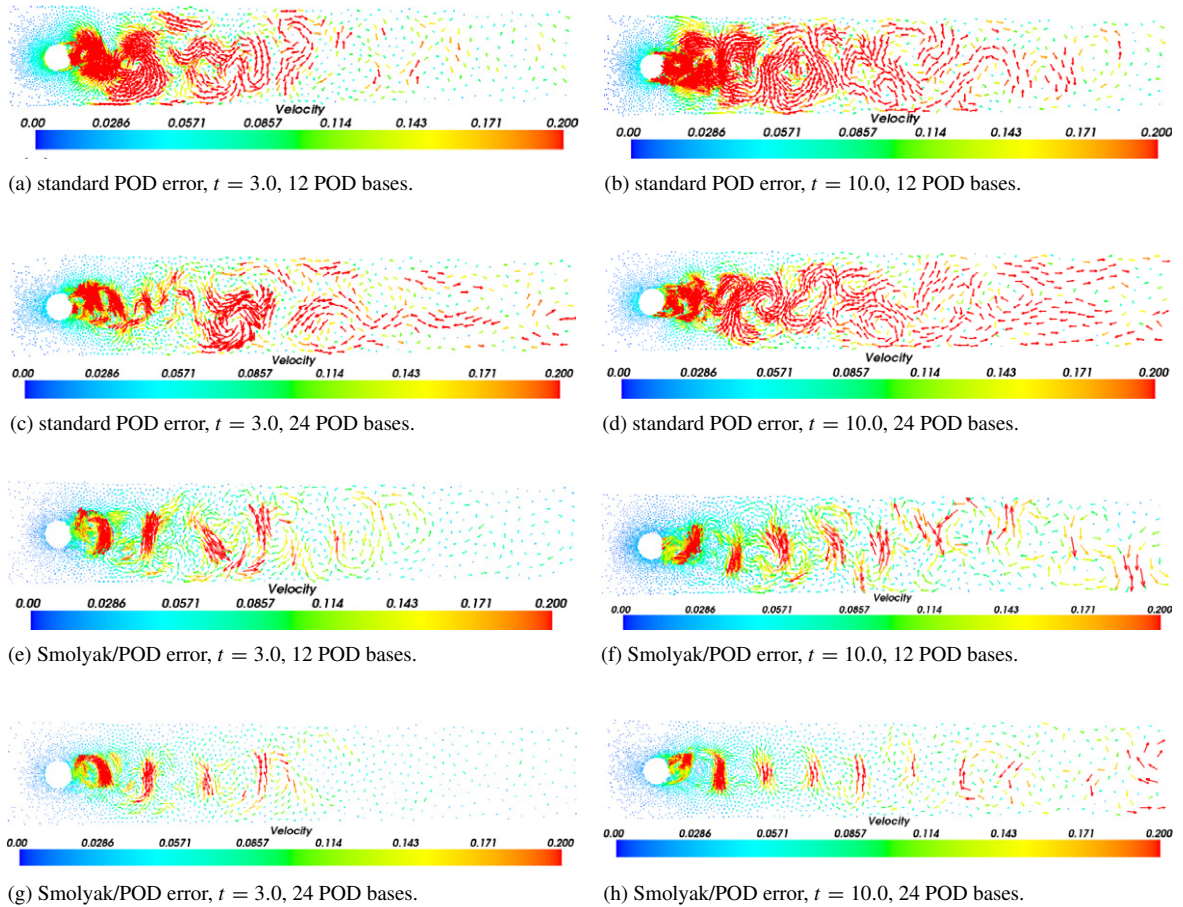
Fig. 5. Case one—flow past a cylinder at $Re = 3600$: The figures displayed above show the solution difference between the full model and the standard POD and the Smolyak sparse grid ROM of the flow past a cylinder problem at time instances 3.0 and 10.0 using 12 POD basis and 24 POD bases.

In this study case, it is demonstrated that the Smolyak sparse grid ROM can reproduce better solutions in comparison with the other POD models for $Re = 400, 3500$. The standard POD model is formed by projecting the full model onto the reduced order space through a Galerkin projection, thus introducing errors into the POD model which may even grow exponentially and have contributed to the poorer performance of the standard POD approach compared with the sparse grid ROM. A new Petrov–Galerkin method was introduced to stabilize the resulting equations and produce more accurate results [15]. Here, we use the standard POD approach. In the Smolyak ROM, the POD coefficients are computed using sparse grid interpolation (see Eq. (28)) where the functional values are calculated accurately from the full model (see Section 4.2). It has been argued by others [45] that 'Smolyak algorithms constitute the ideal blending of different full tensor approximations from the perspective of exact sets; that is, the exact set of the Smolyak algorithm contains the union of the exact sets of the component full tensor approximations'. See also [46]. Also the Smolyak sparse grid ROM with an increase of approximation levels is able to represent not only quadratic (e.g. the Taylor POD ROM proposed here), but also high order non-linearities. These arguments explain why the Smolyak ROM can perform better than other POD ROMs (both intrusive and non-intrusive).

The accuracy of the POD ROM results can be further improved by increasing the number of POD bases. Figs. 6 and 7 compare the full solution and the Smolyak sparse grid non-intrusive reduced order model when using 24 and 35 POD basis functions respectively. In both cases there is a visual improvement in the Smolyak ROM's predictions in comparison to the solutions provided by the standard POD ROM when the same number of basis functions is used. Fig. 8 shows the flow speed at two points in the domain using 12 POD bases and 35 POD bases. It is again shown that the accuracy of velocity solution is improved by increasing the number of POD bases to 35. In this case, the Smolyak

(a) full model, $t = 3.0$.

(b) full model, $t = 10.0$.

(c) standard POD, $t = 3.0$.

(d) standard POD, $t = 10.0$.

(e) Smolyak sparse grid ROM, $t = 3.0$.

(f) Smolyak sparse grid ROM, $t = 10.0$.
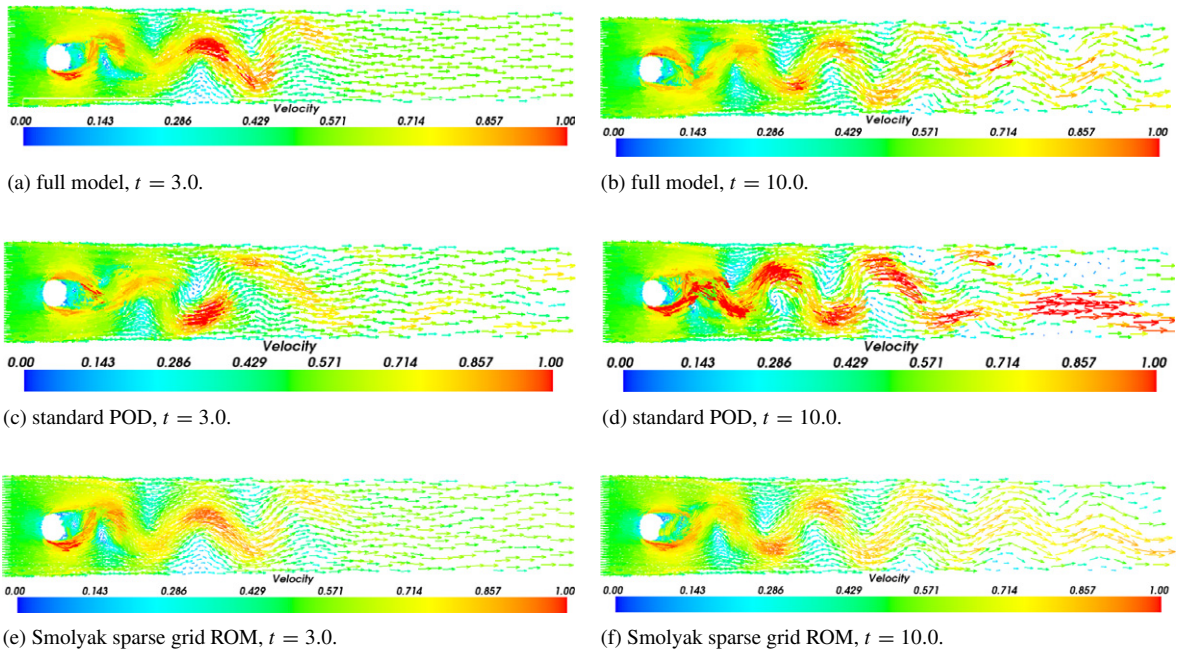
Fig. 6. Case one—flow past a cylinder at $Re = 3600$: The figures displayed above show the solutions of the flow past a cylinder problem at time instances 3.0 and 10.0. The solutions compare the predictions from Smolyak sparse grid non-intrusive ROM using 24 POD basis functions.

(a) full model, $t = 3.0$.

(b) full model, $t = 10.0$.

(c) Standard POD, $t = 3.0$.

(d) Standard POD, $t = 10.0$.

(e) Smolyak sparse grid ROM, $t = 3.0$.

(f) Smolyak sparse grid ROM, $t = 10.0$.
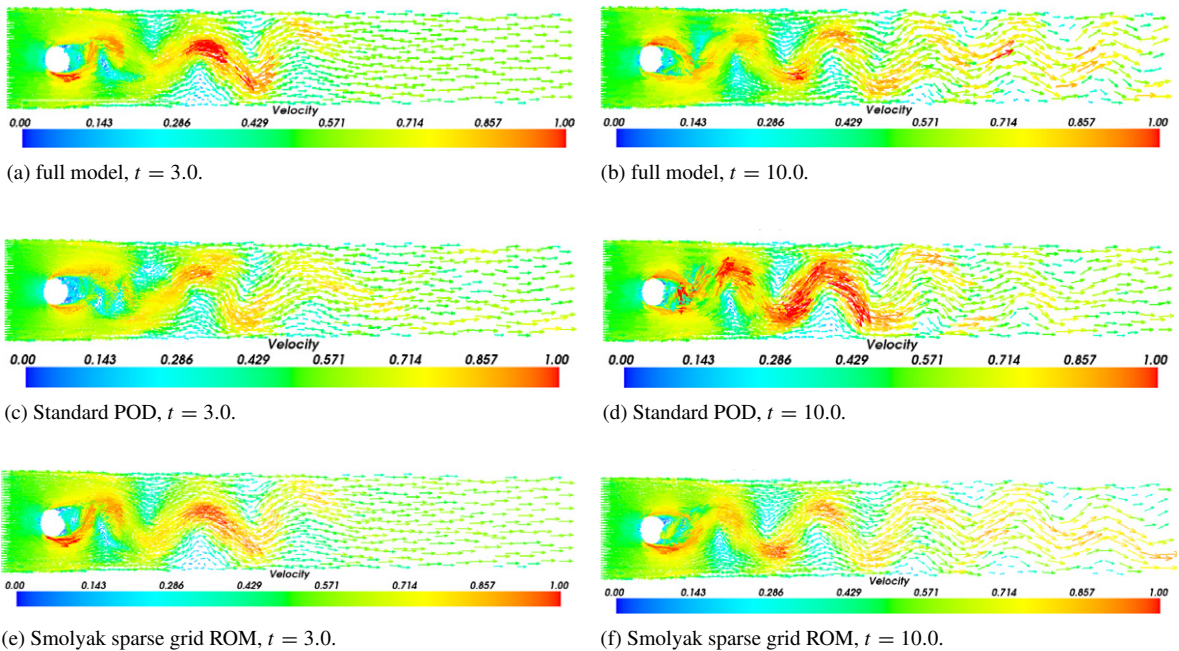
Fig. 7. Case one—flow past a cylinder at $Re = 3600$: The figures displayed above show the solutions of the flow past a cylinder problem at time instances 3.0 and 10.0. The solutions compare the predictions from Smolyak sparse grid non-intrusive ROM using 35 POD basis functions.

sparse grid ROM can perform well only using 12 POD bases when there are no abrupt change in solutions, however, this abrupt change in time can be captured by increasing the number of POD bases, as shown in Fig. 8. It is also seen in Fig. 9 that the RMSE of velocity results obtained from the Smolyak sparse grid ROM decreases as the number of POD bases increases.

(a) Locations a (0.195, 0.267) and b (0.619, 0.298).

(b) Fluid speed at a (0.195, 0.267).

(c) Fluid speed at b (0.619, 0.298).
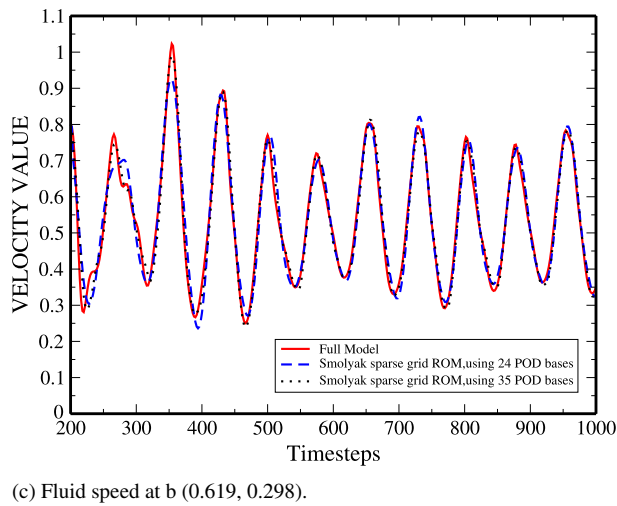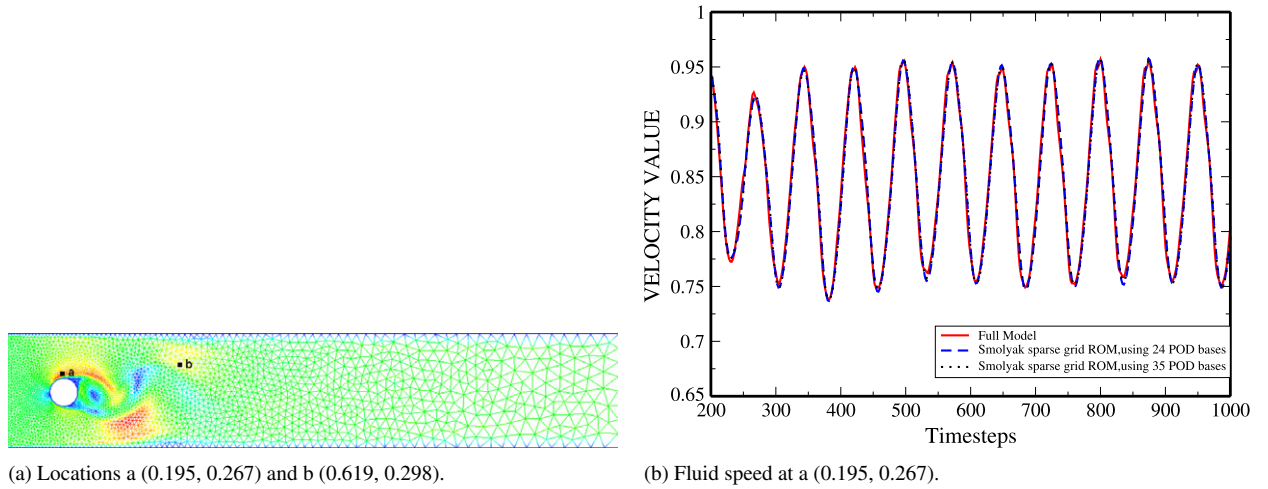
Fig. 8. Case one—flow past a cylinder at $Re = 3600$: The graphs show the flow speed predicted by the full model, and the Smolyak sparse grid ROM at positions a (0.195, 0.267) and b (0.619, 0.298). These results were obtained using a reduced order model with 24 and 35 POD functions.
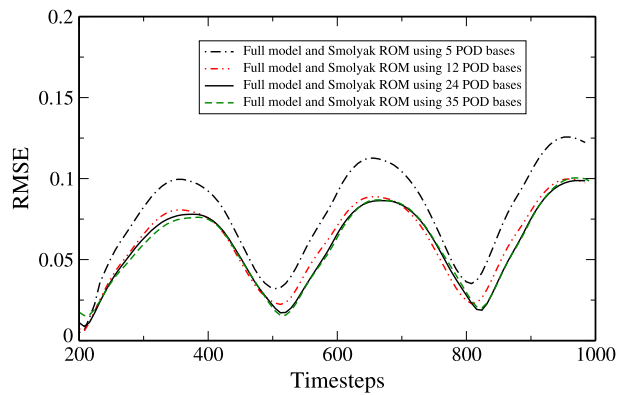
Fig. 9. Case one—flow past a cylinder at $Re = 3600$: The graphs show the RMSE of results obtained from Smolyak ROM.

Fig. 10 compares the full model and Smolyak sparse grid ROM using different sparse grid levels l with $l \in \{0, 1, 2\}$ using 12 POD bases. Each dimension has the number of nodes $n^l = 2^l + 1$ in which l denotes the number of levels.

(a) full model, $t = 6.0$, 12 POD bases.

(b) one level Smolyak grid, $t = 6.0$, 12 POD bases.

(c) zero level Smolyak grid, $t = 6.0$, 12 POD bases.

(d) two level Smolyak grid, $t = 6.0$, 12 POD bases.
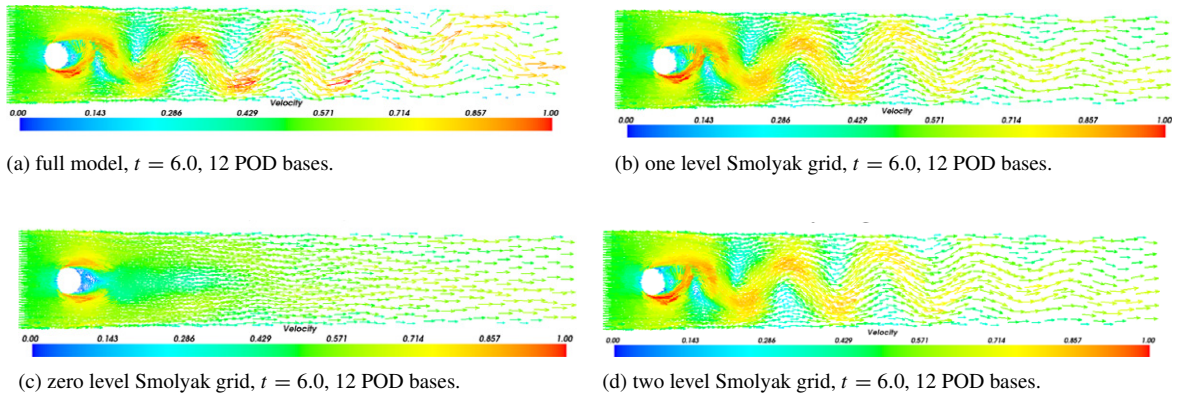
Fig. 10. Case one—flow past a cylinder at $Re = 3600$: The graphs show the comparison between full model with different levels of Smolyak grid using 12 POD bases at $t = 6$.
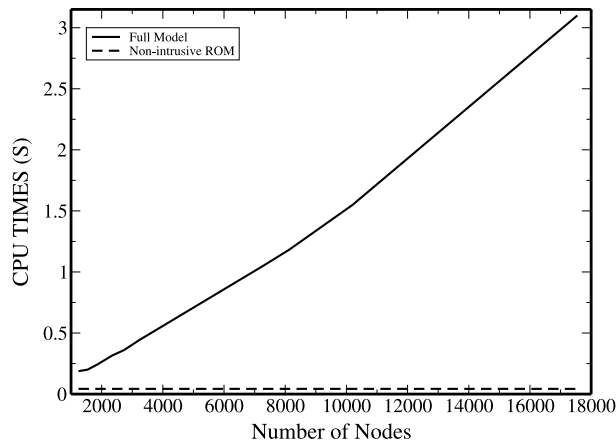
Fig. 11. Case one—flow past a cylinder at $Re = 3600$: Computational times to compute each time step as a function of mesh size (number of nodes) in the full model. Comparisons are made between the full model and the non-intrusive ROM.

As we can see from Fig. 10, even level one (3 points at each dimension) performs well, while level zero (one point at each dimension, mean value of each dimension) failed to capture the energy of the flows.

Fig. 11 shows the online CPU time required to compute a single time step with varying mesh size. The offline CPU time for calculating the Smolyak interpolation functions and the first/second order derivative matrices for the Taylor/POD method are not taken into account. It shows the cost of the ROM models remain static with increased resolution of mesh, and that significant CPU speed-ups are obtained using mesh with the largest number of nodes. For the largest mesh the CPU costs were reduced by a factor of 100 compared to the cost of the high fidelity model. Table 1 shows comparison of the online CPU time required for running the full model and non-intrusive ROMs for each time step. The online CPU time listed here includes the time for assembling and solving the matrix for the full model while interpolating (Smolyak), Matrix multiplication (Taylor) and projecting the POD solution onto the full space for the non-intrusive ROM. In this study case, the CPU time required for matrix multiplication can be ignored since the dimensional size (36×36) of matrices is very small. It can be seen that the non-intrusive ROM is CPU time efficient, since it does not involve assembling and solving the matrices process, thus resulting in a speed-up of CPU time of two orders of magnitude.

5.2. Case 2: The Gyre problem

The second numerical example involves the simulation of a gyre for which a circulating fluid moves across a domain that is 1000×1000 km across and 500 m in depth. The solution's free surface is driven by a wind with a force

Table 1
Case one—flow past a cylinder at $Re = 3600$: Comparison of the online CPU time (dimensionless) required for running the full model and ROM for each time step.

Model	Assembling	Solving	Projection	Interpolation (Smolyak) matrix multiplication (Taylor)	Total
Full model	3.004	0.113	0.000	0.000	3.117
POD ROM	0.303	0.000	0.008	0.000	0.311
Smolyak ROM	0.000	0.000	0.008	0.004	0.012
Taylor/POD	0.000	0.000	0.008	0.000	0.008

strength given by the expression,

$$\tau_y = \tau_0 \cos(\pi y/L) \quad \text{and} \quad \tau_x = 0.0, \tag{31}$$

where L is the system length ($L = 1000$ km). The terms τ_x and τ_y are the wind stresses on the free surface that act along the x and y directions, respectively. In this example the maximum zonal wind stress was set to $\tau_0 = 0.1$ N m^{-1} in the latitude (y) direction. The Coriolis terms are taken into account with the beta-plane approximation ($f = \beta y$) where $\beta = 1.8 \times 10^{-11}$ and the reference density of the fluid is set to $\rho_0 = 1000$ kg m^{-3}. The velocity is 3.5×10^2 m/s^{-1}. With this setup the Reynolds number of the problem was calculated to be $Re = 300$.

The gyre was simulated using a finite element model for a period of 161 days using a time step of $\Delta t = 0.322$ days. From this simulation 500 snapshots of the solution were recorded and from this data 12 POD basis functions were generated. It was found that this POD basis set captured over 99% of the energy of the u, v and p snapshot data. The problem was then re-simulated using the newly developed non-intrusive reduced order model. Fig. 12 shows the velocity profiles obtained from the full model at 41 and 93 days using 6 POD bases. The errors between the full model and the non-intrusive order model are shown at the bottom of Fig. 12. Fig. 13 shows the velocity profiles obtained from the full model at 41 and 93 days using 12 POD bases. The numerical results obtained show that the main gyre is accurately resolved using non-intrusive reduced order model. Fig. 14 shows the RMSE between the full model and the non-intrusive model, which means the solutions of the non-intrusive model are in close agreement with the high-fidelity full model solutions. Fig. 15 displays the correlation coefficient between the full model and the non-intrusive model, this indicates that the RMSE of velocity results obtained from the Smolyak sparse grid model is smaller than that from the standard POD model. The non-intrusive Smolyak sparse grid model exhibits an overall good agreement with the full model. It can be also seen that an increase in the number of POD bases leads an improvement in the accuracy of the POD model—the RMSE of velocity results is decreased.

6. Conclusions

In this article two new non-intrusive reduced order methods are presented. Both methods are based on POD methodologies where optimal basis functions are generated through the method of snapshots. However rather than using a standard Galerkin projection ROM approach (code intrusive), the two approaches based on the Smolyak sparse grid interpolation method and on a second order Taylor series expansion, are employed to calculate the POD coefficients. The method based on Smolyak sparse grid interpolation method constructs a supercube that replaces the governing equations within the reduced space. The other method uses a second order Taylor expansion to capture the quadratic non-linearities in the Navier–Stokes equations. The benefits of the non-intrusive model reduction approaches presented here are that they do not require any modifications to the source code, due to the fact that they are independent of the equation of the system, and simply work from a number of snapshots of the full solution.

The methods have been numerically compared against a finite element unstructured adaptive mesh fluid model (Fluidity) on two flow problems. The two problems were based on the simulation of flow past a cylinder and wind driven gyre respectively. The two non-intrusive methods gave accurate solutions for modelling both flow problems. It is demonstrated that accuracy of solutions from both non-intrusive models is maintained whilst online CPU times are reduced by several orders of magnitude in comparison to high fidelity models. However, for higher Reynolds numbers the Smolyak method was shown to be more robust in maintaining accuracy for resolving the more complex flows. An error analysis has also been carried out for the validation and accuracy assessment of the newly non-intrusive model. The non-intrusive Smolyak sparse grid model exhibits an overall good agreement with the full model. It can

(a) Full model, $t = 41$ days.

(b) Full model, $t = 93$ days.

(c) Smolyak grid ROM, $t = 41$ days.

(d) Smolyak grid ROM, $t = 93$ days.

(e) Error in ROM, $t = 41$ days.

(f) Error in ROM, $t = 93$ days.
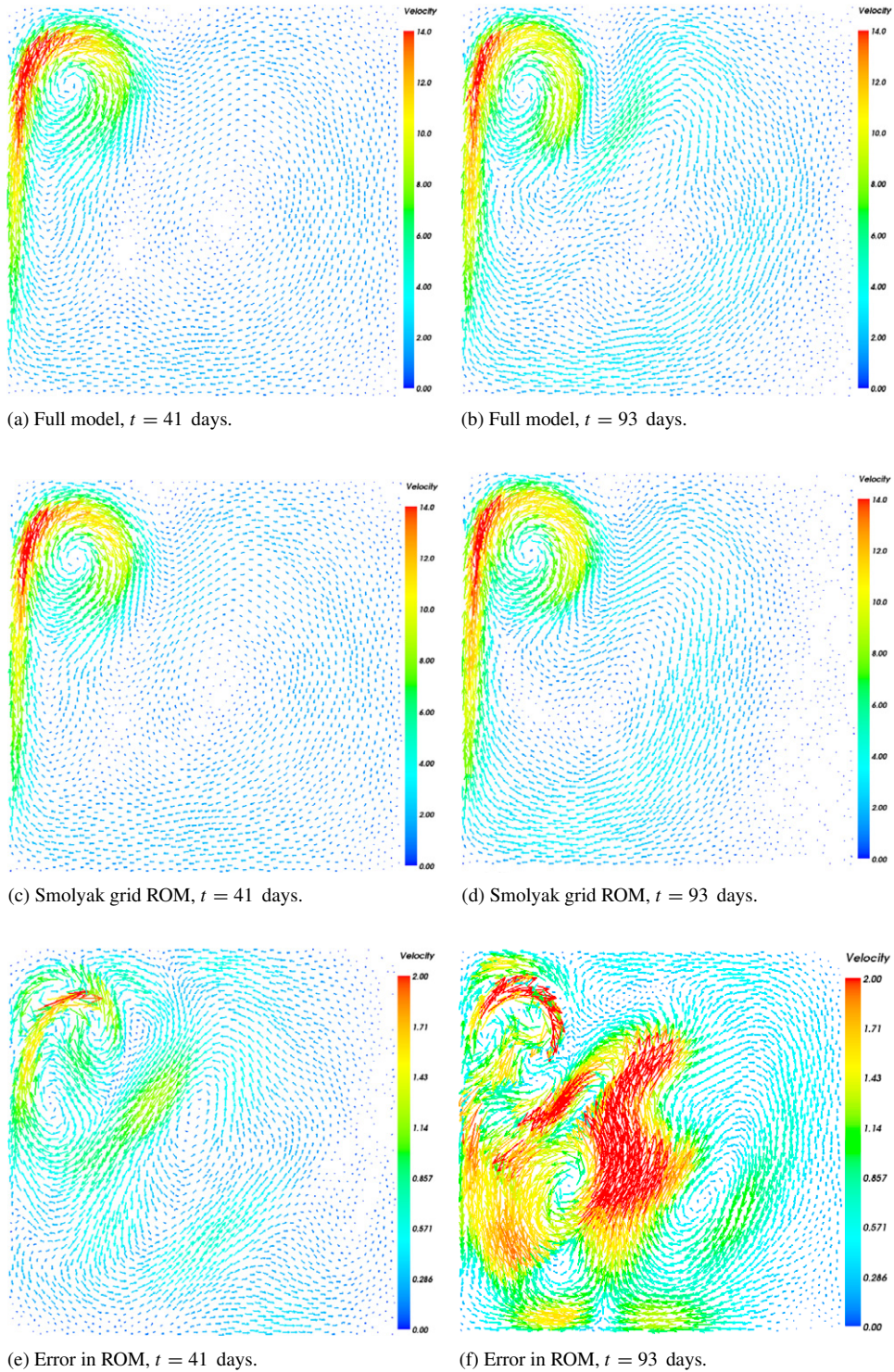
Fig. 12. Case two—gyre: The graphs show the comparison between full model with different levels of Smolyak grid using 12 POD bases at $t = 6$, $Re = 3600$. The figures displayed above show the solutions of the gyre problem at time instance 41 (left) and 93 days (right). The solutions compare the predictions from the full model (top), the Smolyak sparse grid ROM (middle) **using 6 POD functions** (middle). The Figures at the bottom are the difference between full and Smolyak sparse grid ROM.

(a) full model, $t = 41$ days.

(b) full model, $t = 93$ days.

(c) Smolyak grid ROM, $t = 41$ days.

(d) Smolyak grid ROM, $t = 93$ days.

(e) Error in ROM, $t = 41$ days.

(f) Error in ROM, $t = 93$ days.
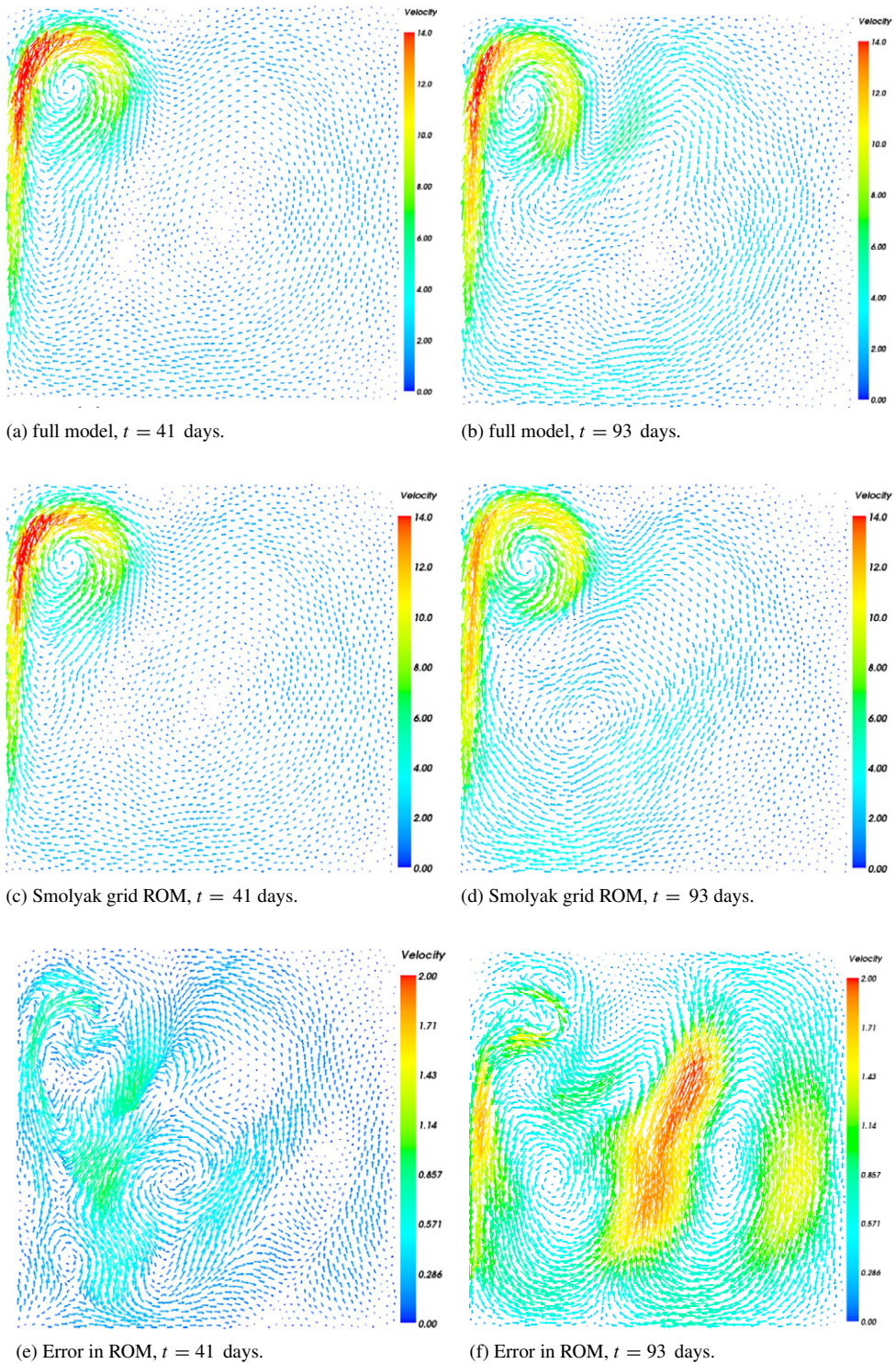
Fig. 13. Case two—gyre: The figures displayed above show the solutions of the gyre problem at time instance 41 (left) and 93 days (right). The solutions compare the predictions from the full model (top), the Smolyak sparse grid ROM (middle) **using 12 POD functions** (middle). The figures at the bottom are the errors between full and Smolyak sparse grid ROM.
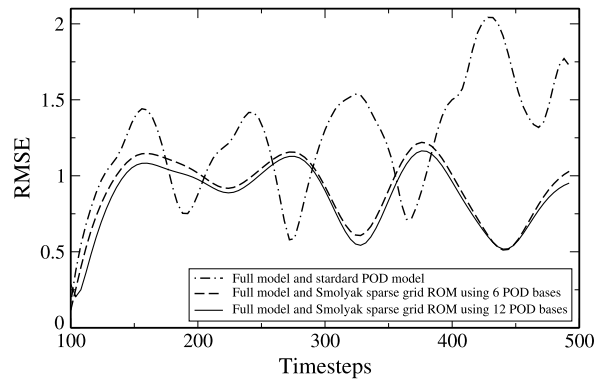
Fig. 14. Case two—gyre: The graph shows the RMSE errors calculated for the Smolyak sparse grid ROM.
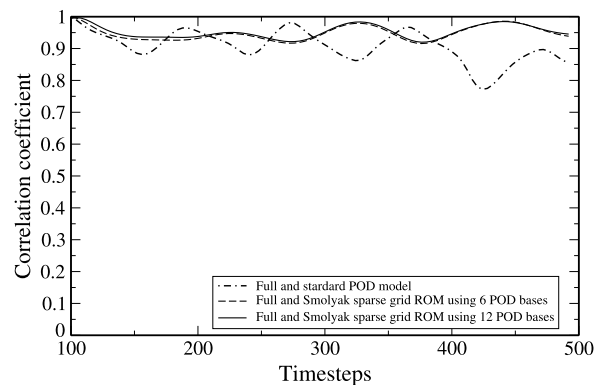
Fig. 15. Case two—gyre: The graph shows the correlation coefficient calculated for the Smolyak sparse grid ROM.

be also seen that an increase in the number of POD bases leads an improvement in the accuracy of the POD model. Future work will investigate the effects of applying this new approach to more complex fluid flows and combining non-intrusive methods with the DEIM methodology (see [24]).

Acknowledgements

References

[1] K. Pearson, On lines and planes of closest fit to systems of points in space, Phil. Mag. 2 (1901) 559–572.
[2] K. Fukunaga, Introduction to statistical recognition, in: Computer Science and Scientific Computing Series, second ed., Academic Press, Boston, MA, 1990, pp. 5–33.
[3] D.T. Crommelin, A.J. Majda, Strategies for model reduction: Comparing different optimal bases, J. Atmospheric Sci. 61 (2004) 2206–2217.
[4] I.T. Jolliffe, Principal Component Analysis, second ed., Springer, 2002, pp. 559–572.
[5] Y. Cao, J. Zhu, I.M. Navon, Z. Luo, A reduced order approach to four dimensional variational data assimilation using proper orthogonal decomposition, Internat. J. Numer. Methods Fluids 53 (2007) 1571–1583.
[6] P.T.M. Vermeulen, A.W. Heemink, Model-reduced variational data assimilation, Mon. Weather Rev. 134 (2006) 2888–2899.

[7] D.N. Daescu, I.M. Navon, A dual-weighted approach to order reduction in 4d-var data assimilation, Mon. Weather Rev. 136 (3) (2008) 1026–1041.

[8] R. Stefanescu, I.M. Navon, POD/DEIM nonlinear model order reduction of an adi implicit shallow water equations model, J. Comput. Phys. 237 (2013) 95–114.

[9] R. Stefanescu, A. Sandu, I.M. Navon, Comparison of POD reduced order strategies for the nonlinear 2D shallow water equations, Int. J. Numer. Methods Fluids 76 (2014) 497–521.

[10] X. Chen, I.M. Navon, F. Fang, A dual-weighted trust-region adaptive pod 4d-var applied to a finite-element shallow-water equations model, Internat. J. Numer. Methods Fluids 65 (5) (2011) 520–541.

[11] X. Chen, S. Akella, I.M. Navon, A dual-weighted trust-region adaptive pod 4-d var applied to a finite-volume shallow water equations model on the sphere, Internat. J. Numer. Methods Fluids 68 (3) (2012) 377–402.

[12] M.U. Altaf, Model reduced variational data assimilation for shallow water flow models (Ph.D. thesis), Delft University of Technology, 2011.

[13] J. Du, F. Fang, C.C. Pain, I.M. Navon, J. Zhu, D.A. Ham, POD reduced-order unstructured mesh modeling applied to 2D and 3D fluid flow, Comput. Math. Appl. 65 (2013) 362–379.

[14] F. Fang, C. Pain, I.M. Navon, A.H. Elsheikh, J. Du, D. Xiao, Non-linear Petrov-Galerkin methods for reduced order hyperbolic equations and discontinuous finite element methods, J. Comput. Phys. 234 (2013) 540–559.

[15] D. Xiao, F. Fang, J. Du, C.C. Pain, I.M. Navon, A.G. Buchan, A.H. ElSheikh, G. Hu, Non-linear Petrov-Galerkin methods for reduced order modelling of the navier-stokes equations using a mixed finite element pair, Comput. Methods Appl. Mech. Eng. 255 (2013) 147–157.

[16] D. Xiao, F. Fang, A.G. Buchan, C.C. Pain, I.M. Navon*, J. Du, G. Hu, Non-linear model reduction for the Navier-Stokes equations using residual deim method, J. Comput. Phys. 263 (2014) 1–18.

[17] H. Chen, Blackbox stencil interpolation method for model reduction (Master's thesis), Massachusetts Institute of Technology, 2012.

[18] B.R. Noack, M. Morzynski, G. Tadmor, Reduced-Order Modelling for Flow Control, vol. 528, Springer, 2011.

[19] R. Noori, A.R. Karbassi, Kh. Ashrafi, M. Ardestani, N. Mehrdadi, Development and application of reduced-order neural network model based on proper orthogonal decomposition for bod5 monitoring: Active and online prediction, Environ. Prog. Sustainable Energy 32 (1) (2013) 120–127.

[20] C. Audouze, F.D. Vuyst, P.B. Nair, Nonintrusive reduced-order modeling of parametrized time-dependent partial differential equations, Numer. Methods Partial Differential Equations 29 (5) (2013) 1587–1628.

[21] E. Iuliano, D. Quagliarella, Aerodynamic shape optimization via non-intrusive pod-based surrogate modelling, in: 2013 IEEE Congress on Evolutionary Computation Cancún, México, 2013, pp. 1–8.

[22] M. Guénot, I. Lepot, C. Sainvitu, J. Goblet, R.F. Coelho, Adaptive sampling strategies for non-intrusive POD-based surrogates, Eng. Comput. 30 (4) (2013) 521–547.

[23] F. Casenave, A. Ern, T. Lelièvre, A nonintrusive reduced basis method applied to aeroacoustic simulations, Adv. Comput. Math. (2014) 1–26.

[24] H. Klie, Unlocking fast reservoir predictions via non-intrusive reduced order models, in: The SPE Reservoir Simulation Symposium held in The Woodland, Texas, USA, 2013, pp. 1–16.

[25] S.A. Smolyak, Quadrature and interpolation formulas for tensor products of certain classes of functions, in: Dokl. Akad. Nauk SSSR, vol. 4, 1963, p. 123.

[26] J. Garcke, M. Griebel, Sparse Grids and Applications, Springer, 2013.

[27] D. Pflüger, B. Peherstorfer, H.J. Bungartz, Spatially adaptive sparse grids for high-dimensional data-driven problems, J. Complexity 26 (5) (2010) 508–522.

[28] J. Burkardt, The sparse grid interpolant, in: Presentation at Department of Scientific Computing, Florida State University, 2012, pp. 1–5.

[29] T. Gerstner, M. Griebel, Numerical integration using sparse grids, Numer. Algorithms 18 (3-4) (1998) 209–232.

[30] F. Nobile, R. Tempone, C.G. Webster, A sparse grid stochastic collocation method for partial differential equations with random input data, SIAM J. Numer. Anal. 46 (5) (2008) 2309–2345.

[31] K.L. Judd, L. Maliar, S. Maliar, R. Valero, Smolyak method for solving dynamic economic models: Lagrange interpolation, anisotropic grid and adaptive domain, J. Econ. Dyn. Control 44 (2014) 92–123.

[32] F. Heiss, V. Winschel, Likelihood approximation by numerical integration on sparse grids, J. Econometrics 144 (1) (2008) 62–80.

[33] N. Ganapathysubramanian, B, Zabaras, Sparse grid collocation schemes for stochastic natural convection problems, J. Comput. Phys. 225 (1) (2007) 652–685.

[34] G.T. Buzzard, D. Xiu, Variance-based global sensitivity analysis via sparse-grid interpolation and cubature, Commun. Comput. Phys. 9 (3) (2011) 542–567.

[35] Angel Gavilan, Juan A. Rojas, Solving Portfolio Problems with the Smolyak-Parameterized Expectations Algorithm. Banco de Espana Working Papers 0838, Banco de Espana, February 2009.

[36] V. Barthelmann, E. Novak, K. Ritter, High dimensional polynomial interpolation on sparse grids, Adv. Comput. Math. 12 (4) (2000) 273–288.

[37] B. Peherstorfer, Model order reduction of parametrized systems with sparse grid learning techniques (Dissertation), Technische Universitat Munchen, Munchen, 2013.

[38] M. Cheng, Adaptive methods exploring intrinsic sparse structures of stochastic partial differential equations (Ph.D. thesis), California Institute of Technology, 2013.

[39] S. Ullmann, J. Lang, POD-Galerkin modeling and sparse-grid collocation for a natural convection problem with stochastic boundary conditions, in: Sparse Grids and Applications-Munich 2012, Springer, 2014, pp. 295–315.

[40] P.S. Sumant, H. Wu, A.C. Cangellaris, N.R. Aluru, A sparse grid based collocation method for model order reduction of finite element approximations of passive electromagnetic devices under uncertainty, in: Microwave Symposium Digest (MTT), 2010 IEEE MTT-S International, IEEE, 2010, pp. 1652–1655.

[41] C.C. Pain, M.D. Piggott, A.J.H. Goddard, et al., Three-dimensional unstructured mesh ocean modelling, Ocean Model. 10 (2005) 5–33.

[42] L. Sirovich, Turbulence and the dynamics of coherent structures, part III: Dynamics and scaling, Q. Appl. Math. XLV (1987) 583–590.

[43] S. Chaturantabut, Dimension reduction for unsteady nonlinear partial differential equations via empirical interpolation methods (Master's thesis), Rice university, 2008.

[44] J. Burkardt, Sparse grid collocation for uncertainty quantification, in: Presentation at Department of Scientific, Computing Florida State University, 2014, pp. 1–64.

[45] P.R. Conrard, Y.M. Marzouk, Adaptive Smolyak pseudospectral approximations, SIAM J. Sci. Comput. 35 (6) (2013) 2643–2670.

[46] M.S. Eldred, J. Burkardt, Comparison of Non-intrusive Polynomial Chaos and Stochastic Collocation Methods for Uncertainty Quantification, American Institute of Aeronautics and Astronautics, 2009, pp. 1–20. 2009–0976.